

Theory of helix traveling wave tubes with dielectric and vane loading

H. P. Freund,^{a)} E. G. Zaidman, and T. M. Antonsen, Jr.^{a),b)}
Naval Research Laboratory, Washington, D.C. 20375

(Received 5 March 1996; accepted 6 May 1996)

A time-dependent nonlinear analysis of a helix traveling wave tube (TWT) is presented for a configuration where an electron beam propagates through a sheath helix surrounded by a conducting wall. The effects of dielectric and vane loading are included in the formulation as is efficiency enhancement by tapering the helix pitch. Dielectric loading is described under the assumption that the gap between the helix and the wall is uniformly filled by a dielectric material. The vane-loading model describes the insertion of an arbitrary number of vanes running the length of the helix, and the polarization of the field between the vanes is assumed to be an azimuthally symmetric transverse-electric mode. The field is represented as a superposition of azimuthally symmetric waves in a vacuum sheath helix. An overall explicit sinusoidal variation of the form $\exp(ikz - i\omega t)$ is assumed (where ω denotes the angular frequency corresponding to the wave number k in the vacuum sheath helix), and the polarization and radial variation of each wave is determined by the boundary conditions in a vacuum sheath helix. The propagation of each wave *in vacuo* as well as the interaction of each wave with the electron beam is included by allowing the amplitudes of the waves to vary in z and t . A dynamical equation for the field amplitudes is derived analogously to Poynting's equation, and solved in conjunction with the three-dimensional Lorentz force equations for an ensemble of electrons. Electron beams with both a continuous and emission-gated pulse format are analyzed, and the model is compared with linear theory of the interaction as well as with the performance of a TWTs operated at the Naval Research Laboratory and at Northrop-Grumman Corporation. © 1996 American Institute of Physics. [S1070-664X(96)02208-2]

I. INTRODUCTION

The development of the traveling wave tube (TWT) extends over several decades since the pioneering work of Pierce and co-workers^{1–3} based upon a coupled-wave analysis utilizing the vacuum modes of the helix and the positive and negative energy space-charge waves of the beam. Improved linear theories based upon an eigenvector analysis of Maxwell's equations in a sheath helix have also been developed,^{4,5} and discussions of both the coupled-wave and field theories of the TWT are given by Beck⁶ and Hutter.⁷ More recently, complete field theories of beam-loaded helix TWTs have been developed for both sheath⁸ and tape⁹ helix models, and dielectric loading has also been incorporated into the sheath helix analyses.¹⁰

Nonlinear theories of the TWT also have a long history in the literature, and can be grouped into two broad classes dealing with steady-state and time-dependent models. Steady-state models have been used to study the growth of a single frequency wave injected simultaneously with the electron beam. These formulations constitute a slow-time-scale approach.^{11–14} A good review of this technique as applied to TWTs has been given by Rowe,¹⁵ and the approach is well suited to the analysis of a broad class of linear beam amplifiers and has also been applied, for example, to the free-electron laser.¹⁶

Time-dependent models of helix TWTs rely upon particle-in-cell (PIC) simulation techniques. At the present time, a one-dimensional PIC simulation code is available,¹⁷

which treats dispersion by means of a transmission line equivalent circuit model. Hence, the one-dimensional PIC simulation of this form is limited in its ability to model the dispersion of the helix and is unable to deal with radial variation in the mode structure. The most general PIC formulations of the interaction in a helix TWT to date are two-dimensional simulations of a sheath helix model.^{18,19} Since the helix is in reality a three-dimensional structure, a two-dimensional PIC formulation requires a prescription for dealing with the boundary condition at the helix. In practice, the simplification made is to treat the so-called *sheath* helix in which the conductivity is infinite in the direction of the helix, and zero otherwise. While this approach can provide a good approximation for the dispersion and radial mode variation in the sheath helix, it is not adaptable to more realistic helix models, which include substantial harmonic components.

The approach we adopt in this paper differs from these PIC formulations. As in the case of the two-dimensional PIC formulations, we assume azimuthal symmetry and deal with a sheath helix model. However, we treat the fields in terms of a spectral decomposition in which the electromagnetic field is expressed as a superposition of the normal modes of the vacuum sheath helix. In this representation, an overall sinusoidal variation of the form $\exp(ikz - i\omega t)$ is assumed for each wave, where ω denotes the angular frequency determined from the vacuum sheath helix dispersion equation corresponding to wave number k . The polarization and radial variation of each wave is assumed to be given by the normal mode solutions of Maxwell's equations for the vacuum sheath helix boundary conditions, which are three-dimensional in nature. The evolution of each wave either *in vacuo* or in the presence of the electron beam is included by

^{a)}Science Applications International Corp., McLean, Virginia 22102.

^{b)}University of Maryland, College Park, Maryland 20742.

allowing the amplitudes to vary in both axial position and time. The detailed evolution of the waves is governed by a dynamical equation that is analogous to Poynting's equation. This equation includes the coupling of the waves to the electron beam and, hence, the intermodulation between the waves themselves. In conjunction with the equations for the fields, the trajectories of an ensemble of electrons are integrated using the three-dimensional Lorentz force equations.

As in the case of the two-dimensional PIC formulations, this spectral approach provides a good model for the dispersion and radial variation of the electromagnetic field, but requires an explicit choice of the waves of interest to be specified as an initial condition. It has two advantages over the two-dimensional PIC models, however, in that (1) the technique can be readily generalized to deal with more realistic tape helix models, which include higher harmonic components; and (2) the numerical technique is considerably less computationally demanding. For the numerical examples discussed in this paper, typical run times on a Cray Y-MP supercomputer were substantially less than one minute.

One restriction that is imposed in the present analysis is the neglect of the beam space-charge modes that restricts the analysis to the ballistic regime in which the Pierce gain parameter² is small. The exclusion of the space-charge modes is not an essential element of the formulation, and the inclusion of the space-charge modes is presently under study. The self-electric and self-magnetic fields have also been neglected. However, the self-fields can be readily included by means of a technique used for inclusion of the self-fields in free-electron lasers.²⁰

The numerical examples discussed herein relate to the single-pass propagation of pulses through both vacuum and beam-loaded helix structures, and open boundary conditions have been imposed. However, various degrees of reflecting boundary conditions can also be used to treat various cavity and oscillator configurations. Finally, the formulation can also be generalized to treat more realistic helix models; in particular, a tape helix model is presently under study.⁹

The organization of the paper is as follows. The general formulation is presented in Sec. II. This includes a discussion of the geometry, the dispersion equation and mode structure in a sheath helix, the field representation and the dynamical equation governing the evolution of the fields, and the Lorentz force equations. In Sec. III we deal with the numerical techniques used to solve the dynamical equations as well as the representative solutions for various parameter regimes. A summary and discussion is given in Sec. IV.

II. THE GENERAL FORMULATION

The general formulation treats the propagation of multiple waves through a dielectric- and vane-loaded sheath helix in the presence of an electron beam. This is a fully time-dependent problem, and the electron beam model can represent either a continuous or prebunched pulse format. The prebunched electron beam is referred to in the literature as an *emission-gated beam*. In addition, we permit the injected radiation to have an arbitrary format; that is, we can inject either a definite radiation pulse or a continuous signal.

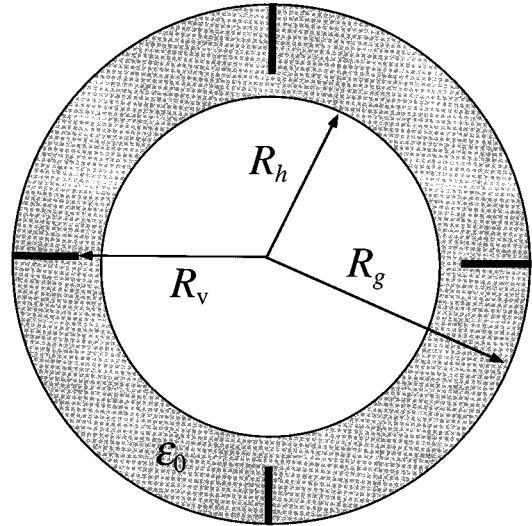


FIG. 1. Schematic representation of the cross section of the helix circuit.

A. The helix circuit configuration

The physical configuration that is treated is that of an energetic electron beam propagating parallel to the axis of symmetry of a dielectric and vane-loaded helix. Azimuthal symmetry is assumed throughout. A schematic of the cross section of the helix circuit is shown in Fig. 1, in which the vanes are positioned radially, and where R_h and R_g are used to denote the radii of the helix and the outer cylinder, R_v denotes the inner radius of the vanes, and ϵ_0 is the dielectric constant.

In practical TWTs the helix is composed of a metal strip or wire that is supported at multiple points within the cylinder by posts or rods. A complete self-consistent description of wave dispersion in such a structure is beyond the scope of the present analysis. For simplicity, we assume that both the helix and the outer cylinder are loss-free conductors and represent the electromagnetic field as a superposition of the azimuthally symmetric modes in the vacuum helix. Within the context of this assumption, there are several further simplifications that permit an analytic solution for the normal modes of the vacuum helix.

In the commonly applied *tape* helix model, it is assumed that only a surface current is induced in the helix and that the effects of the support posts can be neglected. The restriction to surface currents in the helix is equivalent to the assumption that the helix is "thin" in the radial direction. A schematic illustration of a "tape" helix is shown in Fig. 2, where R_h is the helix radius, λ_h denotes the helix period and δ_h is the width of the tape. The unit vector describing the pitch of the helix is $\hat{\mathbf{e}}_\phi = \hat{\mathbf{e}}_\theta \cos \phi + \hat{\mathbf{e}}_z \sin \phi$, where $\tan \phi = 1/k_h R_h$ for a helix wave number $k_h (\equiv 2\pi/\lambda_h)$. A multiplicity of azimuthally symmetric modes exist in such a system corresponding to the spatial harmonics of the helix period. The importance of the higher-order spatial harmonics decreases as the width of the helix increases. Ultimately, if $\delta_h = \lambda_h$, the induced currents in the helix can be modeled as a continuous helical current sheet, and the effects of the spatial harmonics disappear. This is referred to as the *sheath* helix approxima-

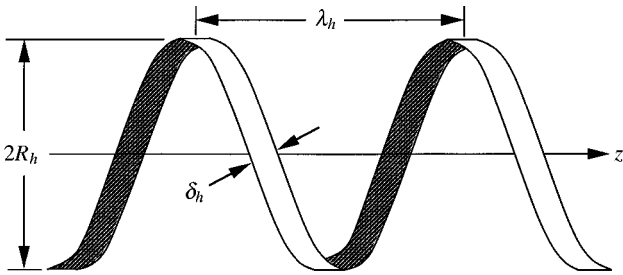


FIG. 2. Schematic illustration of a tape helix structure.

tion. For simplicity, we shall adopt a sheath helix model for the electromagnetic fields, but observe that the general technique we describe is readily generalizable to a tape helix model.

B. The modes in a sheath helix

We restrict the analysis to the azimuthally symmetric subluminous waves supported by the circuit. The azimuthally symmetric electric and magnetic fields can be represented in the form (see the Appendix)

$$\begin{aligned} \delta\mathbf{E}(\mathbf{x},t) = & \sum_n \delta\hat{E}_n \{ R_n(r) \hat{\mathbf{e}}_r \sin(\varphi_n + \delta\varphi_n) \\ & - [\beta_{ph}(k_n) \Theta_n(r) \hat{\mathbf{e}}_\theta - Z_n^{(e)}(r) \hat{\mathbf{e}}_z] \cos(\varphi_n \\ & + \delta\varphi_n) \}, \\ \delta\mathbf{B}(\mathbf{x},t) = & \sum_n \delta\hat{E}_n \{ \Theta_n(r) \hat{\mathbf{e}}_r \cos(\varphi_n + \delta\varphi_n) \\ & + [\beta_{ph}(k_n) R_n(r) \hat{\mathbf{e}}_\theta - Z_n^{(b)}(r) \hat{\mathbf{e}}_z] \sin(\varphi_n \\ & + \delta\varphi_n) \}, \end{aligned} \quad (1)$$

where the summation is over the modes to be included, and $\delta\hat{E}_n$ denotes the wave amplitudes. The phase is composed of two parts: one given by the phase of the wave propagating in the cold vacuum helix given by $\varphi_n \equiv k_n z - \omega_n t$ for wave number $k_n \equiv n \Delta k$ and angular frequency ω_n , such that (k_n, ω_n) satisfy the vacuum sheath helix dispersion equation and Δk is the separation in wave number between the waves, and a part governed by the interaction with the electron beam $\delta\varphi_n$. We assume that both $\delta\hat{E}_n$ and $\delta\varphi_n$ vary in z and t . In addition, $\beta_{ph}(k_n) \equiv v_{ph}(k_n)/c = \omega_n/c k_n$ denotes the normalized phase velocity of each wave. The vacuum sheath helix dispersion equation is (see the Appendix)

$$\frac{\omega_n^2}{c^2} - \frac{p_n q_n}{k_h^2 R_h^2} \frac{J_0(p_n R_h)}{J_1(p_n R_h)} \frac{W_{0,0}(q_n R_v, q_n R_h)}{W_{1,1}(q_n R_v, q_n R_h)} \frac{[p_n J_0(p_n R_h) W_{1,1}(q_n R_g, q_n R_h) - q_n J_1(p_n R_h) W_{1,0}(q_n R_g, q_n R_h)]}{[q_n J_1(p_n R_h) W_{0,0}(q_n R_v, q_n R_h) + \epsilon_0 p_n J_0(p_n R_h) W_{1,0}(q_n R_h, q_n R_v)]} = 0, \quad (2)$$

where $k_h (\equiv 2\pi/\lambda_h)$ is the helix wave number, $p_n^2 \equiv \omega_n^2/c^2 - k_n^2$, $q_n^2 \equiv \epsilon_0 \omega_n^2/c^2 - k_n^2$, $W_{m,n}(x,y) \equiv Y_m(x) J_n(y) - J_m(x) Y_n(y)$, and J_n and Y_n denote the Bessel and Neumann functions. The components of the polarization vectors depend upon the frequency, wave number, and dimensions of the helix and outer cylinder, and are given by

$$R_n(r) = \begin{cases} \frac{k_n}{p_n} J_1(p_n r); & \text{I}, \\ -\frac{k_n}{q_n} J_0(p_n R_h) \frac{W_{1,0}(q_n r, q_n R_v)}{W_{0,0}(q_n R_v, q_n R_h)}; & \text{II}, \\ 0; & \text{III}, \end{cases} \quad (3)$$

$$\Theta_n(r) = \frac{ck_n/\omega_n}{k_h R_h} \begin{cases} \frac{J_0(p_n R_h) J_1(p_n r)}{J_1(p_n R_h)}; & \text{I}, \\ \frac{q_n}{p_n} J_0(p_n R_h) \frac{W_{1,1}(q_n R_g, q_n r)}{W_{1,1}(q_n R_g, q_n R_h)}; & \text{II and III}, \end{cases} \quad (4)$$

$$Z_n^{(e)}(r) = \begin{cases} J_0(p_n r); & \text{I}, \\ J_0(p_n R_h) \frac{W_{0,0}(q_n R_v, q_n r)}{W_{0,0}(q_n R_v, q_n R_h)}; & \text{II}, \\ 0; & \text{III}, \end{cases} \quad (5)$$

$$Z_n^{(b)}(r) = \frac{cp_n/\omega_n}{k_h R_h} \begin{cases} \frac{J_0(p_n R_h) J_0(p_n r)}{J_1(p_n R_h)}; & \text{I}, \\ \frac{q_n}{p_n} J_0(p_n R_h) \frac{W_{1,0}(q_n R_g, q_n r)}{W_{1,1}(q_n R_g, q_n R_h)}; & \text{II and III}, \end{cases} \quad (6)$$

where region I denotes $0 \leq r < R_h$, region II denotes $R_h \leq r < R_v$, and region III denotes $R_v \leq r \leq R_g$.

It should be noted here that within the vanes in region III the field is azimuthally symmetric, and that $\delta E_r = \delta E_z = \delta B_\theta = 0$. In general, the field within the vanes (and, by extension, the overall field) will contain azimuthal harmonics based upon the number of vanes and the vane spacing. However, we have assumed azimuthal symmetry; this restricts the analysis to the lowest-order azimuthal harmonic, which displays a simple transverse-electric polarization within the vanes.

Energy transport for each wave within the vacuum helix/cylinder is determined by the Poynting flux, the stored energy density, and the group velocity. The Poynting flux for each wave denotes the time-averaged power flux over the entire cross section of the cylinder and helix, and using the fields given in Eqs. (1) can be expressed as

$$S_n = P_n \delta \hat{E}_n^2, \quad (7)$$

where

$$\begin{aligned} P_n = & \frac{k_n \omega_n R_h^2}{8 p_n^2} \left\{ \left(1 - \frac{\epsilon_0 p_n^2}{q_n^2} \right) J_0^2(p_n R_h) + \left(J_1^2(p_n R_h) - \frac{\epsilon_0 p_n^2}{q_n^2} J_0^2(p_n R_h) \right) \frac{W_{1,0}^2(q_n R_h, q_n R_v)}{W_{0,0}^2(q_n R_v, q_n R_h)} \right. \\ & - J_0^2(p_n R_h) \frac{W_{1,0}^2(q_n R_g, q_n R_h)}{W_{1,1}^2(q_n R_g, q_n R_h)} \Big] - \frac{2 J_0(p_n R_h)}{p_n R_h} \left(J_1(p_n R_h) + \frac{\epsilon_0 p_n^3}{q_n^3} J_0(p_n R_h) \right) \frac{W_{1,0}(q_n R_h, q_n R_v)}{W_{0,0}(q_n R_v, q_n R_h)} \\ & - \frac{c^2 p_n^2}{\omega_n^2} \frac{2}{k_h^2 R_h^2} \frac{J_0(p_n R_h)}{p_n R_h} \left(\frac{J_0^2(p_n R_h)}{J_1(p_n R_h)} - \frac{p_n}{q_n} J_0(p_n R_h) \right) \frac{W_{1,0}(q_n R_g, q_n R_h)}{W_{1,1}(q_n R_g, q_n R_h)} \\ & \left. + \frac{\tan^2 \phi}{W_{1,1}^2(q_n R_g, q_n R_h)} \right). \end{aligned} \quad (8)$$

In addition, the time-averaged energy density per unit axial length over the entire cross section of the helix and cylinder is given by

$$W_n = U_n \delta \hat{E}_n^2, \quad (9)$$

where

$$\begin{aligned} U_n = & \frac{\omega_n}{k_n c^2} P_n + \frac{R_h}{4 p_n} J_0(p_n R_h) \left(J_1(p_n R_h) + \frac{\epsilon_0 p_n}{q_n} J_0(p_n R_h) \right) \frac{W_{1,0}(q_n R_h, q_n R_v)}{W_{0,0}(q_n R_v, q_n R_h)} + \frac{R_h^2(\epsilon_0 - 1)}{8} J_0^2(p_n R_h) \\ & \times \left[\frac{4}{\pi^2 q_n^2 R_h^2} \left(\frac{\epsilon_0 \omega_n^2 / c^2 q_n^2}{W_{0,0}^2(q_n R_v, q_n R_h)} + \frac{\tan^2 \phi}{W_{1,1}^2(q_n R_g, q_n R_h)} \right) - \left(\frac{\epsilon_0 \omega_n^2}{c^2 q_n^2} + \tan^2 \phi \right) - \left(\frac{\epsilon_0 \omega_n^2}{c^2 q_n^2} \frac{W_{1,0}^2(q_n R_h, q_n R_v)}{W_{0,0}^2(q_n R_v, q_n R_h)} \right. \right. \\ & \left. \left. + \tan^2 \phi \frac{W_{1,0}^2(q_n R_g, q_n R_h)}{W_{1,1}^2(q_n R_g, q_n R_h)} \right) - \frac{2}{q_n R_h} \left(\frac{\epsilon_0 \omega_n^2}{c^2 q_n^2} \frac{W_{1,0}(q_n R_h, q_n R_v)}{W_{0,0}(q_n R_v, q_n R_h)} - \tan^2 \phi \frac{W_{1,0}(q_n R_g, q_n R_h)}{W_{1,1}(q_n R_g, q_n R_h)} \right) \right]. \end{aligned} \quad (10)$$

Finally, the group velocity of each individual wave is given by

$$v_{\text{gr}}(k_n) \equiv \frac{\partial \omega_n}{\partial k_n} = \frac{P_n}{U_n}. \quad (11)$$

For convenience, we rewrite the electric and magnetic fields in the form

$$\delta \mathbf{E}(\mathbf{x}, t) = \sum_n [\delta \hat{E}_n^{(1)} \mathbf{e}_n(\mathbf{x}, t) + \delta \hat{E}_n^{(2)} \mathbf{e}_n^*(\mathbf{x}, t)], \quad (12)$$

$$\delta \mathbf{B}(\mathbf{x}, t) = \sum_n [\delta \hat{E}_n^{(1)} \mathbf{b}_n(\mathbf{x}, t) + \delta \hat{E}_n^{(2)} \mathbf{b}_n^*(\mathbf{x}, t)],$$

where $\delta \hat{E}_n^{(1)} = \delta \hat{E}_n \cos \delta \varphi_n$ and $\delta \hat{E}_n^{(2)} = \delta \hat{E}_n \sin \delta \varphi_n$, and the polarization vectors are given in cylindrical coordinates by

$$\begin{aligned} \mathbf{e}_n(\mathbf{x}, t) = & \{ R_n(r) \hat{\mathbf{e}}_r \sin \varphi_n - [\beta_{\text{ph}}(k_n) \Theta_n(r) \hat{\mathbf{e}}_\theta \\ & - Z_n^{(e)}(r) \hat{\mathbf{e}}_z] \cos \varphi_n \}, \end{aligned}$$

$$\begin{aligned} \mathbf{b}_n(\mathbf{x}, t) = & \{ \Theta_n(r) \hat{\mathbf{e}}_r \cos \varphi_n + [\beta_{\text{ph}}(k_n) R_n(r) \hat{\mathbf{e}}_\theta \\ & - Z_n^{(b)}(r) \hat{\mathbf{e}}_z] \sin \varphi_n \}, \end{aligned} \quad (13)$$

$$\begin{aligned} \mathbf{e}_n^*(\mathbf{x}, t) = & \{ R_n(r) \hat{\mathbf{e}}_r \cos \varphi_n + [\beta_{\text{ph}}(k_n) \Theta_n(r) \hat{\mathbf{e}}_\theta \\ & - Z_n^{(e)}(r) \hat{\mathbf{e}}_z] \sin \varphi_n \}, \end{aligned}$$

$$\begin{aligned} \mathbf{b}_n^*(\mathbf{x}, t) = & \{ -\Theta_n(r) \hat{\mathbf{e}}_r \sin \varphi_n + [\beta_{\text{ph}}(k_n) R_n(r) \hat{\mathbf{e}}_\theta \\ & - Z_n^{(b)}(r) \hat{\mathbf{e}}_z] \cos \varphi_n \}. \end{aligned}$$

Observe that the polarization vectors satisfy the source-free Maxwell equations; hence

$$\nabla \times \mathbf{e}_n = -\frac{1}{c} \frac{\partial}{\partial t} \mathbf{b}_n \quad \text{and} \quad \nabla \times \mathbf{b}_n = \frac{1}{c} \frac{\partial}{\partial t} \mathbf{e}_n, \quad (14)$$

as well as

$$\nabla \times \mathbf{e}_n^* = -\frac{1}{c} \frac{\partial}{\partial t} \mathbf{b}_n^* \quad \text{and} \quad \nabla \times \mathbf{b}_n^* = \frac{1}{c} \frac{\partial}{\partial t} \mathbf{e}_n^*. \quad (15)$$

C. The dynamical equations for the fields

In order to treat the variation in the radial mode structure as well as the axial and temporal evolution of the wave(s), we represent the electromagnetic field in terms of the superposition given in Eqs. (12) under the assumption that the mode amplitudes vary more slowly in z and t [i.e., $\delta\hat{E}_n^{(1)} = \delta\hat{E}_n^{(1)}(z, t)$, and $\delta\hat{E}_n^{(2)} = \delta\hat{E}_n^{(2)}(z, t)$]. This spatial and temporal variation in the wave amplitudes describes the propagation of a pulse through either a vacuum helix or in the presence of an electron beam subject to (1) the dispersion of the waves in a sheath helix, and (2) the variations in the radial inhomogeneities of each wave with frequency.

The dynamical equations for the wave amplitudes are obtained in a manner analogous to the derivation of Poynting's theorem. Bearing in mind that $\mathbf{e}_n(\mathbf{x}, t)$ and $\mathbf{b}_n(\mathbf{x}, t)$ satisfy Maxwell equations in the absence of a source, Ampère's law is of the form

$$\begin{aligned} & \sum_n \left(\hat{\mathbf{e}}_z \times \mathbf{b}_n \frac{\partial}{\partial z} \delta\hat{E}_n^{(1)} - \mathbf{e}_n \frac{\partial}{\partial t} \delta\hat{E}_n^{(1)} \right) \\ & + \sum_n \left(\hat{\mathbf{e}}_z \times \mathbf{b}_n^* \frac{\partial}{\partial z} \delta\hat{E}_n^{(2)} - \mathbf{e}_n^* \frac{\partial}{\partial t} \delta\hat{E}_n^{(2)} \right) \\ & = \frac{4\pi}{c} \mathbf{J}(\mathbf{x}, t), \end{aligned} \quad (16)$$

and Faraday's law is

$$\begin{aligned} & \sum_n \left(\hat{\mathbf{e}}_z \times \mathbf{e}_n \frac{\partial}{\partial z} \delta\hat{E}_n^{(1)} + \mathbf{b}_n \frac{\partial}{\partial t} \delta\hat{E}_n^{(1)} \right) \\ & + \sum_n \left(\hat{\mathbf{e}}_z \times \mathbf{e}_n^* \frac{\partial}{\partial z} \delta\hat{E}_n^{(2)} + \mathbf{b}_n^* \frac{\partial}{\partial t} \delta\hat{E}_n^{(2)} \right) = 0, \end{aligned} \quad (17)$$

where $\mathbf{J}(\mathbf{x}, t)$ denotes the microscopic source current. The dynamical equations for the fields are obtained in a manner analogous to the derivation of Poynting's equation by (1) taking the inner product of \mathbf{b}_m (and \mathbf{b}_m^*) with Faraday's law (17) and \mathbf{e}_m (and \mathbf{e}_m^*) with Ampère's law (16); (2) subtracting the equations; (3) integrating the result over the entire cross section of the helix and cylinder; and (4) averaging the result over the axial length $2\pi/\Delta k$. Observe that for a single wave, this scale length is just the wavelength. The average diagonalizes the equations so that the evolution of each $\delta\hat{E}_n^{(i)}$ satisfies equations of the form

$$\begin{aligned} \left(\frac{\partial}{\partial t} + v_{\text{gr}}(k_n) \frac{\partial}{\partial z} \right) \delta\hat{E}_n^{(1)} &= \frac{2\Delta k}{cU_n} \int_0^{2\pi/\Delta k} dz' \iint_{A_h} dx dy \mathbf{J}(x, y, z', t) \cdot \mathbf{e}_n(x, y, z', t), \\ \left(\frac{\partial}{\partial t} + v_{\text{gr}}(k_n) \frac{\partial}{\partial z} \right) \delta\hat{E}_n^{(2)} &= \frac{2\Delta k}{cU_n} \int_0^{2\pi/\Delta k} dz' \iint_{A_h} dx dy \mathbf{J}(x, y, z', t) \cdot \mathbf{e}_n^*(x, y, z', t), \end{aligned} \quad (18)$$

where A_h denotes the cross-sectional area enclosed by the helix. This equation describes the propagation of a pulse, or pulses, through the helix/cylinder at the appropriate group velocities. Intermodulation between the various waves is implicitly included through the particle trajectories.

D. The case of a tapered helix

This model can be adapted to treat the case of a helix with a spatially varying period by the relatively simple expedient of allowing the helix wave number to vary in z and recalculating the wave number, group velocity, and the Poynting flux, and energy density of each wave as a function of axial position. In so doing, we neglect any reflected waves that might result from the tapered helix. In practice, this is equivalent to the assumption that the variation in the wavelength that results from the tapered helix period varies slowly in comparison with the wavelengths of interest; hence, $\lambda \gg \Delta z(d\lambda/dz)$.

Using this procedure, we observe that there will be a gradient in the vacuum fields \mathbf{e}_n and \mathbf{b}_m due to the taper. As a result, the vacuum fields satisfy the modified equations

$$\nabla \times \mathbf{e}_n + \frac{1}{c} \frac{\partial}{\partial t} \mathbf{b}_n = h_n, \quad (19)$$

$$\nabla \times \mathbf{b}_n - \frac{1}{c} \frac{\partial}{\partial t} \mathbf{e}_n = g_n, \quad (20)$$

$$\nabla \times \mathbf{e}_n^* + \frac{1}{c} \frac{\partial}{\partial t} \mathbf{b}_n^* = h_n^*, \quad (21)$$

$$\nabla \times \mathbf{b}_n^* - \frac{1}{c} \frac{\partial}{\partial t} \mathbf{e}_n^* = g_n^*, \quad (22)$$

where

$$\mathbf{h}_n(\mathbf{x}, t) \equiv \frac{\partial(\beta_{\text{ph}} \Theta_n)}{\partial z} \hat{\mathbf{e}}_r \cos \varphi_n - \frac{\partial R_n}{\partial z} \hat{\mathbf{e}}_\theta \sin \varphi_n, \quad (23)$$

$$\mathbf{g}_n(\mathbf{x}, t) \equiv \frac{\partial(\beta_{\text{ph}} R_n)}{\partial z} \hat{\mathbf{e}}_r \sin \varphi_n - \frac{\partial \Theta_n}{\partial z} \hat{\mathbf{e}}_\theta \cos \varphi_n, \quad (24)$$

$$\mathbf{h}_n^*(\mathbf{x}, t) \equiv -\frac{\partial(\beta_{\text{ph}} \Theta_n)}{\partial z} \hat{\mathbf{e}}_r \sin \varphi_n + \frac{\partial R_n}{\partial z} \hat{\mathbf{e}}_\theta \cos \varphi_n, \quad (25)$$

$$\mathbf{g}_n^*(\mathbf{x}, t) \equiv \frac{\partial(\beta_{\text{ph}} R_n)}{\partial z} \hat{\mathbf{e}}_r \cos \varphi_n + \frac{\partial \Theta_n}{\partial z} \hat{\mathbf{e}}_\theta \sin \varphi_n, \quad (26)$$

and this reflects the effect of the variation in the wave number with axial position on the polarization vectors. Following the same procedure outlined above, we find that the dynamical equations for a tapered helix can be expressed in the relatively simple form

$$\begin{aligned} \left(\frac{\partial}{\partial t} + v_{\text{gr}}(k_n) \frac{\partial}{\partial z} \right) (P_n^{1/2} \delta \hat{E}_n^{(1)}) &= \frac{2 \Delta k P_n^{1/2}}{c U_n} \int_0^{2\pi/\Delta k} dz' \int_{A_h} \int dx dy \mathbf{J}(x, y, z', t) \cdot \mathbf{e}_n(x, y, z', t), \\ \left(\frac{\partial}{\partial t} + v_{\text{gr}}(k_n) \frac{\partial}{\partial z} \right) (P_n^{1/2} \delta \hat{E}_n^{(2)}) &= \frac{2 \Delta k P_n^{1/2}}{c U_n} \int_0^{2\pi/\Delta k} dz' \int_{A_h} \int dx dy \mathbf{J}(x, y, z', t) \cdot \mathbf{e}_n^*(x, y, z', t). \end{aligned} \quad (27)$$

E. Electron dynamics

The electron dynamics are treated using the full three-dimensional relativistic Lorentz force equations. Azimuthal symmetry is imposed in the sense (1) that the beam distribution upon entry to the helix is azimuthally symmetric, and (2) that each of the vector components of the electromagnetic fields varies only in (r, z, t) . With this in mind, we integrate the Lorentz force equation for each electron in the simulation subject to both the external axial magnetic field and the electromagnetic fields. Hence

$$\frac{d}{dt} \mathbf{p} = -e \delta \mathbf{E}(\mathbf{x}, t) - \frac{e}{c} \mathbf{v} \times [B_0 \hat{\mathbf{e}}_z + \delta \mathbf{B}(\mathbf{x}, t)]. \quad (28)$$

The initial conditions on the ensemble of electrons reflects the specific pulse structure of interest. Thus, electrons are injected into the interaction region at uniform time intervals for a continuous beam, and at periodic but nonuniform intervals for an emission-gated beam. The specific algorithms used for these purposes are described in the following section.

One important restriction in the present analysis is that the fluctuating rf space-charge fields are not explicitly included. Hence, the analysis is strictly valid only subject to the neglect of the positive and negative beam space-charge waves (i.e., the ballistic regime in which the Pierce gain parameter is small). Similarly, the effect of the dc self-electric and self-magnetic fields are also neglected. The inclusion of the rf space-charge and dc self-fields are presently under study.

III. NUMERICAL ANALYSIS

Equations (18) [or (27) for a tapered helix] are solved for a system of length L on a grid with spacing Δz over a time step Δt using the MacCormack method.²¹ The microscopic source current is represented as

$$\begin{aligned} \mathbf{J}(\mathbf{x}, t) &= -q \sum_{i=1}^N v_i(t) \delta[x - x_i(t)] \delta[y - y_i(t)] \\ &\quad \times S[z - z_i(t)], \end{aligned} \quad (29)$$

where N is the number of electrons in the system at time t , $(\mathbf{x}_i, \mathbf{v}_i)$ represents the location and velocity of the i th electron at time t , q is the charge per electron, and S is the shape function. The *shape function* describes the interpolation of the electron charge to the grid locations. We use a triangular shape algorithm,

$$S(z - z_i) = \begin{cases} \frac{z - z_i + \Delta z}{\Delta z^2}; & z_i - \Delta z \leq z \leq z_i, \\ -\frac{z - z_i - \Delta z}{\Delta z^2}; & z_i < z \leq z_i + \Delta z, \end{cases} \quad (30)$$

which provides a linear weighting in which the charge is mapped onto the two nearest neighbor grid points. The charge per electron includes a weight factor dependent upon the beam current. Since we are injecting electrons on each time step, we choose

$$q = \frac{I_b \Delta t}{N_{\Delta t}}, \quad (31)$$

where I_b is the beam current injected over each specific time step and $N_{\Delta t}$ is the number of electrons injected per time step. Note that the charge per electron injected during each time step is found using the average current for a continuous beam, while this current will vary depending upon the bunch shape for an emission-gated beam. As a result, the dynamical equations for the field amplitudes are

$$\begin{aligned} \left(\frac{\partial}{\partial t} + v_{\text{gr}}(k_n) \frac{\partial}{\partial z} \right) (P_n^{1/2} \delta \hat{E}_n^{(1)}) &= -\frac{2q \Delta k P_n^{1/2}}{c U_n} \sum_{i=1}^N \int_0^{2\pi/\Delta k} dz' S(z' - z_i) \mathbf{v}_i(t) \\ &\quad \times \mathbf{J}(x, y, z', t) \cdot \mathbf{e}_n(x, y, z', t) \end{aligned}$$

$$\begin{aligned}
& \cdot \mathbf{e}_n(x_i, y_i, z', t), \\
& \left(\frac{\partial}{\partial t} + v_{\text{gr}}(k_n) \frac{\partial}{\partial z} \right) (P_n^{1/2} \delta \hat{E}_n^{(2)}) \\
& = - \frac{2q \Delta k P_n^{1/2}}{c U_n} \sum_{i=1}^N \int_0^{2\pi/\Delta k} dz' S(z' - z_i) \mathbf{v}_i(t) \\
& \cdot \mathbf{e}_n^*(x_i, y_i, z', t). \tag{32}
\end{aligned}$$

Open boundary conditions for the field are imposed at both $z=0$ and L .

The orbit equations are integrated by means of a fourth-order Runge–Kutta algorithm. In order to be consistent with the electron shape function that maps electron charge onto the grid, we use a linear interpolation scheme to map the field amplitude from the grid to the particle locations.

The sequence of operations used in integrating the field and orbit equations are as follows. We first calculate the sources by accumulating electron charge to the grid and averaging over the appropriate scale length and then step the fields using the MacCormack method. Once the updated fields are calculated, we then step the electron trajectories. This procedure is repeated over the time scale of interest.

A. Injection of electromagnetic waves

TWTs are typically operated as amplifiers in which the electron beam has a continuous pulse format and an injected signal is amplified over the length of the helix. In order to model this configuration, we must specify an algorithm for the injection of a signal(s). For this purpose, we can inject a pulse with arbitrary start, rise, flat and fall times in the following way. We assume that a pulse is injected at $z = -\Delta z$ and allowed to propagate into the interaction region. The pulse has a smooth temporal shape given by

$$\delta \hat{E}_n^{(1)}(z = -\Delta z, t) = \delta \hat{E}_0^{(1)} \begin{cases} 0; & t < \tau_{\text{start}}, \\ \sin^2\left(\frac{\pi}{2} \frac{(t - \tau_{\text{start}})}{\Delta \tau_{\text{rise}}}\right); & \tau_{\text{start}} \leq t < \tau_{\text{rise}}, \\ 1; & \tau_{\text{rise}} \leq t < \tau_{\text{flat}}, \\ \cos^2\left(\frac{\pi}{2} \frac{(t - \tau_{\text{flat}})}{\Delta \tau_{\text{fall}}}\right); & \tau_{\text{flat}} \leq t \leq \tau_{\text{fall}}, \\ 0; & t > \tau_{\text{fall}}, \end{cases} \tag{33}$$

and $\delta \hat{E}_n^{(2)}(z = -\Delta z, t) = 0$ for all t , where $\delta \hat{E}_0^{(1)}$ is chosen to describe the peak power via Eq. (7), τ_{start} denotes the start time of the pulse, $\Delta \tau_{\text{rise}}$ is the rise time of the pulse, $\tau_{\text{rise}} = \tau_{\text{start}} + \Delta \tau_{\text{rise}}$ is the time at which the pulse has risen to its peak value, $\tau_{\text{flat}} - \tau_{\text{rise}}$ is the time interval over which the pulse retains a constant magnitude, $\Delta \tau_{\text{fall}}$ is the time interval over which the pulse falls to zero, and $\tau_{\text{fall}} = \tau_{\text{flat}} + \Delta \tau_{\text{fall}}$ is the time after which the injected pulse vanishes. Note that the injection of power at $z = -\Delta z$ requires the inclusion of a guard cell in the grid outside the interaction region.

Observe that this form gives us great flexibility in the pulse format. For example, a square pulse can be injected by

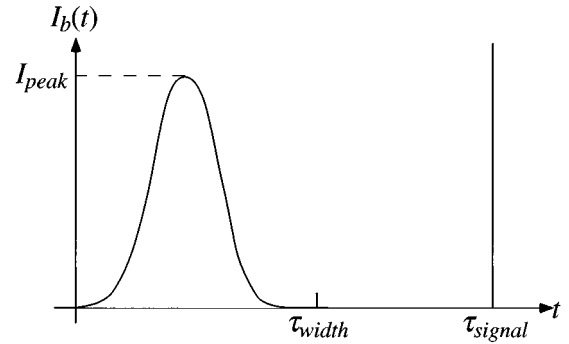


FIG. 3. Schematic illustration of the pulse shape in an emission-gated beam.

the simple expedient of allowing $\Delta \tau_{\text{rise}} = \Delta \tau_{\text{fall}} = 0$, and a constant drive power can be imposed by the further requirement that τ_{flat} equal the entire pulse time. In addition, a single well-defined pulse can be injected by requiring that $\Delta \tau_{\text{rise}} = \Delta \tau_{\text{fall}}$ and that $\tau_{\text{flat}} = \tau_{\text{rise}}$. This same model is used for the injection of either single or multiple waves.

B. Injection of the electron beam

The models of electron injection are chosen to correspond to either a continuous electron beam or an emission-gated beam. In the case of the continuous pulse, electrons are injected at the start of each time step. The charge per electron is calculated using Eq. (31) and we allow for an arbitrary current rise time by choosing a current of the form

$$I_b(t) = \begin{cases} I_b \sin^2\left(\frac{\pi}{2} \frac{t}{\tau_r}\right); & t \leq \tau_r, \\ I_b; & t > \tau_r, \end{cases} \tag{34}$$

where τ_r denotes the rise time of the beam.

A schematic for a single beam pulse for an emission-gated beam is shown in Fig. 3. In the case of an emission-gated beam, bunching is assumed to occur prior to injection into the helix. This may be accomplished, for example, by a periodic signal applied to a gridded cathode. The detailed pulse shape we use is one in which beam pulses repeat over a period τ_{signal} ($\equiv 1/f$, where f is the signal frequency), and in which the beam is “on” only over a time τ_{width} ($\leq \tau_{\text{signal}}$). This is illustrated schematically in Fig. 3. The detailed shape of the current pulse used for the emission over each wave period is

$$I_b(t) = \begin{cases} I_{\text{peak}} \sin^2\left(\frac{\pi}{2} \frac{t}{\tau_{\text{width}}}\right); & 0 \leq t \leq \tau_{\text{width}}, \\ 0; & \tau_{\text{width}} < t \leq \tau_{\text{signal}}. \end{cases} \tag{35}$$

The average current for this specific beam pulse shape is given by

$$\frac{I_{\text{avg}}}{I_{\text{peak}}} = \frac{\tau_{\text{width}}}{2 \tau_{\text{signal}}}, \tag{36}$$

so that the width of the pulse can be determined by the specification of the frequency of the bunching and the ratio of the average to peak currents. Note that no drive power is required for the electromagnetic waves for the emission-gated beam.

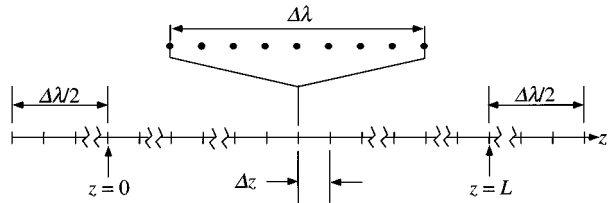


FIG. 4. Schematic illustration of the mapping of charge to the grid and the current average.

As mentioned previously, the sources are determined by first mapping the charge from each electron to the two nearest-neighbor grid points and then averaged over a length $\Delta\lambda$. The specific procedure we employ for this is a “moving-window” average in which the sources at the i th grid cell are determined by averaging over those grid cells within a length $\pm\Delta\lambda/2$ on either side. For example, if $\Delta z=\Delta\lambda/N$ for N even, then the sources at the i th grid cell are determined by averaging the charge over all grid cells within $i\pm N/2$. This necessitates the inclusion of $N/2$ guard cells corresponding to $z<0$ and $z>L$. Thus, electrons are injected at $z=-\Delta\lambda/2$ and allowed to propagate ballistically until they reach $z=0$, at which point the interaction with the radiation is “turned on.” Similarly, the electrons also propagate ballistically (i.e., the interaction with the radiation is “turned off”) when the electrons exit the interaction region at $z=L$. This is illustrated schematically in Fig. 4. Electrons are ejected from the simulation whenever they pass beyond $z=L+\Delta\lambda/2$ or intersect the radial position of the helix. This procedure is also employed in the case of a tapered helix with the generalization that the averaging length varies with axial position corresponding to the variation in the wavelength(s).

One further point deserves mention before we turn to a discussion of the results of the simulation. Since charge is mapped onto the two nearest neighbor grid cells, the end cells of the average corresponding to the i th grid cell (i.e., the grid cells at $i\pm N/2$) will contain contributions from charges outside the length $\Delta\lambda$. This introduces an additional oscillation with a period of $\Delta\lambda+2\Delta z$ into the sources that must be filtered out.

C. Propagation in a vacuum helix

We first consider propagation of a single pulse through the vacuum helix (i.e., in the absence of the electron beam). The circuit parameters we choose to study correspond to a helix TWT built at Northrop–Grumman Corp.²² A schematic of the cross section of this tube is shown in Fig. 5. The helix and wall radii were 0.12446 and 0.2794 cm, respectively, and the helix period was 0.080 137 cm. The helix was supported by three dielectric rods with rectangular cross sections running the length of the helix. The dielectric constant of the rods was 6.5 and the rod dimensions were 0.0508 cm \times 0.147 32 cm. No vanes were used in this structure.

The cold dispersion solutions have been compared with the measured dispersion of this TWT. In order to test the utility of the present model in describing a real circuit, we varied ϵ_0 in the present model to determine the level of agreement that could be achieved over a broad bandwidth.

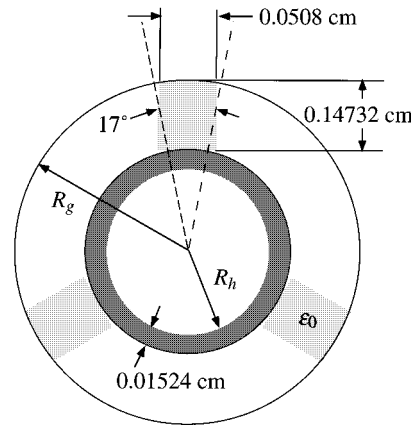


FIG. 5. Schematic illustration of the Northrop–Grumman helix TWT.

The results of this comparison were discussed in detail in a prior publication¹⁰ and are shown in Fig. 6, where we plot the variation in the phase velocity versus frequency as calculated using the cold helix dispersion equation (2) and as measured (dots) over frequencies up to 7.5 GHz for $\epsilon_0=1.75$. It is evident from the figure that the agreement is very good over a broadband of frequencies extending from 3 up to 7 GHz, and we conclude that the effect of the dielectric rods can be modeled using the uniform dielectric loading with an effective dielectric constant of 1.75.

The effective dielectric constant used above can be estimated in a straightforward manner under the assumptions that the effect of the rods do not greatly perturb the field structures and that the field is approximately parallel to the rods. As such, the effective dielectric constant can be determined from an estimate of the energy densities in the stored fields in the vacuum and the dielectric, and the effective dielectric constant is given by a volume-weighted average in which $\epsilon_{\text{eff}} \approx (V_{\text{rod}}\epsilon_{\text{rod}} + V_{\text{vac}})/V_{\text{tot}}$, where V_{rod} and ϵ_{rod} are the volume and dielectric constant of the rod, V_{vac} is the volume of the vacuum in the gap between the helix and the outer wall, and V_{tot} is the total volume in the gap between the helix and the wall. Of course, this formula is expected to yield only an approximation to the effective dielectric constant.

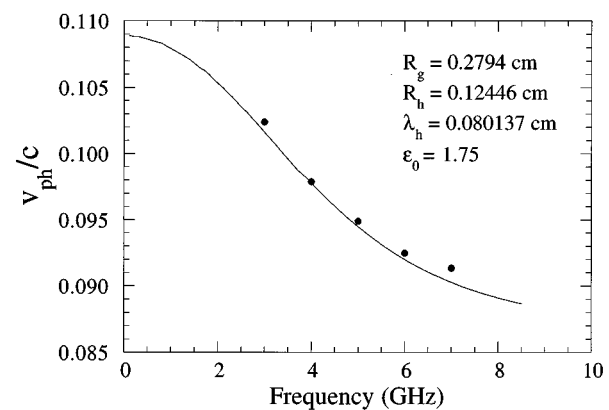


FIG. 6. Comparison of the dispersion in the cold Northrop–Grumman circuit with the solution of the cold helix dispersion equation.

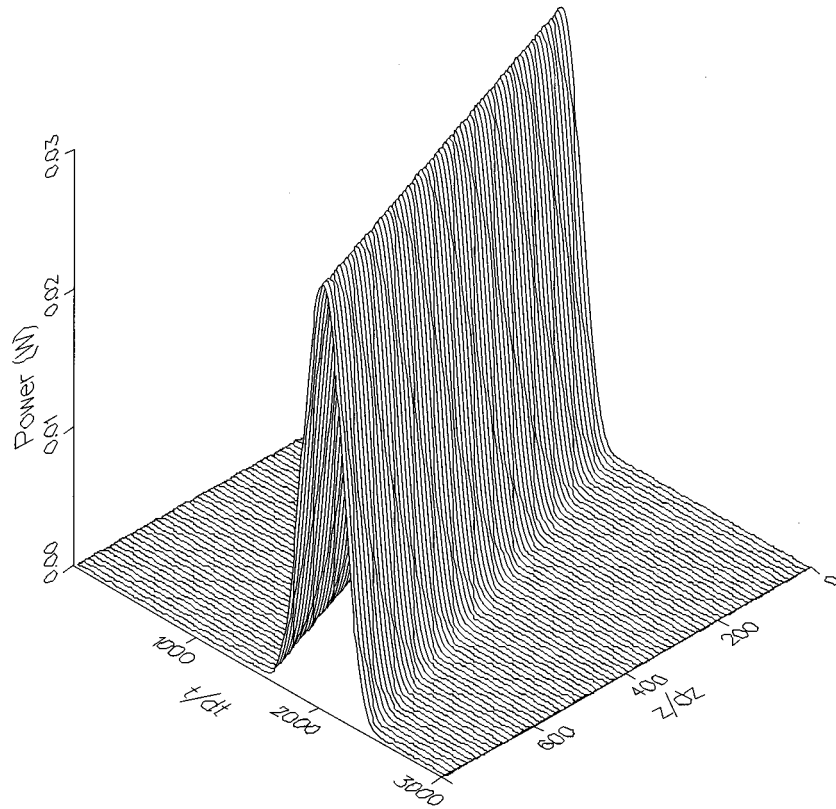


FIG. 7. Perspective plot of the propagation of a pulse through a vacuum helix.

For the parameters of interest, however, we find that $\epsilon_{\text{eff}} \approx 1.66$, which is reasonably close to the value of 1.75 found above.

In propagating a pulse through this helix, we inject a signal with a pulse shape given in Eq. (33) at $t=0$ with a frequency of 5 GHz and a peak power level of 30 mW and a rise and fall time of 1 ns (note that this implies that $\tau_{\text{start}}=0$, $\Delta\tau_{\text{rise}}=\Delta\tau_{\text{fall}}=\tau_{\text{rise}}=\tau_{\text{flat}}=1$ ns, and $\tau_{\text{fall}}=2$ ns). A perspective plot showing the propagation of this pulse through the helix versus both z and t is shown in Fig. 7. It is evident from the figure that the pulse propagates through the helix at the group velocity and with negligible distortion.

D. Continuous beam case—Uniform helix

The continuous beam example we consider corresponds to the TWT built at Northrop–Grumman discussed previously in regard to the propagation of a pulse through the

vacuum helix. Gain was measured in this TWT over a frequency range of 3–7 GHz using a 2.84 kV/0.17 A electron beam with a radius of 0.0495 cm. However, direct comparison of the measured gain of this tube with the nonlinear theory is not possible since space-charge effects were important but are not presently included in the nonlinear formulation. A linear theory of the interaction, which did include space-charge effects, however, was in substantial agreement with the observed gain.¹⁰ Hence, we choose to compare the results of the nonlinear simulation for these helix/beam parameters with the aforementioned linear theory subject to the neglect of the space-charge contribution. This will give us a measure of the accuracy of the nonlinear formulation in the absence of space-charge forces.

The linear dispersion equation in the absence of vane loading is of the form¹⁰

$$\Lambda(\omega, k)\epsilon_{\text{sc}}(\omega, k) = -\frac{\omega_b^2\sigma_b}{4\gamma_0^2c^2}\frac{\omega^2}{c^2}p^2\frac{J_0^2(pR_b)}{J_0(pR_h)J_0(pR_g)}W_{0,0}(pR_g, pR_h), \quad (37)$$

where this describes the case of an annular electron beam with a radius R_b and a thickness ΔR_b , $\sigma_b = 2\pi R_b \Delta R_b$ is the cross-sectional area of the beam, ω_b is the beam plasma frequency, $\gamma_0 = (1 - v_b^2/c^2)^{-1/2}$,

$$\Lambda(\omega, k) \equiv \frac{\omega^2}{c^2} \frac{pq}{k_h^2 R_h^2} \frac{J_0(pR_h)}{J_1(pR_h)} \frac{W_{0,0}(qR_g, qR_h)}{W_{1,1}(qR_g, qR_h)} \frac{[pJ_0(pR_h)W_{1,1}(qR_g, qR_h) - qJ_1(pR_h)W_{1,0}(qR_g, qR_h)]}{[qJ_1(pR_h)W_{0,0}(qR_g, qR_h) + \epsilon_0 p J_0(pR_h)W_{1,0}(qR_h, qR_g)]}, \quad (38)$$

describes the vacuum helix dispersion function, and

$$\epsilon_{sc}(\omega, k) \equiv \frac{\Delta\omega^2}{c^2} - \frac{\omega_b^2 \sigma_b}{4 \gamma_0^2 c^2} p^2 \frac{J_0(pR_b)}{J_0(pR_h)} W_{0,0}(pR_b, pR_h), \quad (39)$$

describes the dielectric function of the beam space-charge waves for $\Delta\omega = \omega - kv_b$ corresponding to a beam velocity v_b . This linear theory corresponds to the case of a strongly magnetized beam.

Equation (37) describes the interaction in terms of the coupling of the vacuum helix mode with the beam space-charge mode. It can be expressed in the conventional form of the Pierce dispersion equation by making a near-resonant approximation in which $\omega \approx kv_b$ after which we obtain

$$(k^2 - k_0^2)[\Delta\omega^2 - 4QC^3 k^2 v_b^2] = 2C^3 \omega k_0 k v_b, \quad (40)$$

where

$$k_0^2 \equiv \frac{\omega^2}{c^2} \left(1 - k_h^2 R_h^2 \frac{p_e}{q_e} \frac{J_1(p_e R_h)}{J_0(p_e R_h)} \frac{W_{1,1}(q_e R_g, q_e R_h)}{W_{0,0}(q_e R_g, q_e R_h)} \frac{[q_e J_1(p_e R_h) W_{0,0}(q_e R_g, q_e R_h) + \epsilon_0 p_e J_0(p_e R_h) W_{1,0}(q_e R_g, q_e R_h)]}{[p_e J_0(p_e R_h) W_{1,1}(q_e R_g, q_e R_h) - q_e J_1(p_e R_h) W_{1,0}(q_e R_g, q_e R_h)]} \right), \quad (41)$$

describes the wave number in the vacuum helix, $p_e = i\omega/\gamma_0 v_b$, $q_e = i\omega(1 - \epsilon_0 v_b^2/c^2)^{1/2}/v_b$, and the Pierce Q and C parameters are given by

$$C^3 \equiv -\frac{\omega_b^2 \sigma_b}{4\pi \gamma_0^4 c^2} \frac{k_h^2 R_h^2}{p_e R_h} \frac{J_0^2(p_e R_h)}{J_0^2(p_e R_h)} \frac{p_e J_1(p_e R_h) W_{1,1}(q_e R_g, q_e R_h)}{p_e J_0(p_e R_h) W_{1,1}(q_e R_g, q_e R_h) - q_e J_1(p_e R_h) W_{1,0}(q_e R_g, q_e R_h)}, \quad (42)$$

$$Q \equiv \frac{\pi}{4\beta_0^2} \frac{p_e R_h}{k_h^2 R_h^2} \frac{J_0(p_e R_h)}{J_0(p_e R_h)} W_{0,0}(p_e R_b, p_e R_h) \frac{p_e J_0(p_e R_h) W_{1,1}(q_e R_g, q_e R_h) - q_e J_1(p_e R_h) W_{1,0}(q_e R_g, q_e R_h)}{p_e J_1(p_e R_h) W_{1,1}(q_e R_g, q_e R_h)}, \quad (43)$$

and $\beta_0 \equiv v_b/c$. Space-charge effects can be neglected when $|\Delta\omega^2| \gg 4|QC^3 k^2 v_b^2|$ and the term in QC^3 can be neglected. Physically, this corresponds to the regime in which the space-charge potential is too weak to significantly modify the effect of the vacuum helix wave on the electron trajectories. Solution of the dispersion equation indicates that the space-charge forces can be neglected when the Q and C parameters satisfy the inequality⁸

$$|C^3| \ll \frac{(1 + 8|Q|)^2}{4|Q|}. \quad (44)$$

Calculation indicates that this condition is not satisfied in the Northrop–Grumman TWT, and that space-charge forces are important in the description of that tube.

The effect of space charge on gain of the Northrop–Grumman TWT can also be gauged by comparison of the linear growth rate as calculated by the complete dispersion equation (37) and by a reduced dispersion equation found by neglecting the space-charge terms. This reduced dispersion equation is found in the limit in which $\epsilon_{sc} \rightarrow \Delta\omega^2/c^2$, and is equivalent to the neglect of the terms in QC^3 in the reduced Pierce form of the dispersion equation. This dispersion equation is of the form

$$\Lambda(\omega, k) = -\frac{\omega_b^2 \sigma_b}{4 \gamma_0^2 c^2} \frac{\omega^2}{\Delta\omega^2} p^2 \frac{J_0^2(pR_b)}{J_0(pR_h) J_0(pR_g)} \times W_{0,0}(pR_g, pR_h). \quad (45)$$

Collective space-charge effects generally act to reduce the gain of a device since they degrade the interaction between the beam and the vacuum mode, and this case is no exception.

The maximum gain, both as calculated by the general dispersion equation (37) and measured in the TWT, is approximately 6.1 dB/cm at a frequency of 5.4 GHz. In contrast, the solution of the dispersion equation (45) in the absence of space-charge forces yields a maximum gain of 7.5 dB/cm at a frequency of 4.5 GHz.

In addition to obtaining the linear growth rate from Eq. (45), we can also estimate the nonlinear efficiency by phase trapping arguments. Specifically, that at saturation the beam electrons will lose an amount of energy corresponding to a deceleration of $2\Delta v$, where $\Delta v = v_b - v_{ph}$ and v_{ph} is the phase velocity of the wave. This technique was originally formulated by Slater for traveling wave tubes,²³ but has also been used successfully for free-electron lasers¹⁶ and gives a predicted efficiency of

$$\eta \approx \frac{2\gamma^3}{\gamma-1} \frac{v_b}{c} \left(\frac{v_b}{c} - \frac{v_{ph}}{c} \right). \quad (46)$$

Hence, the solution of Eq. (45) in the presence of the beam will also allow us to estimate the nonlinear efficiency.

A plot of the solution of Eq. (45) for the gain and efficiency corresponding to the Northrop–Grumman parameters is shown in Fig. 8. Since this is an annular beam theory, we have chosen to use the rms beam radius (0.035 cm). As shown in the figure, gain is found over frequencies up to 7 GHz, with the peak gain of approximately 7.5 dB/cm occurring at a frequency of about 4.5 GHz. The efficiency increases with frequency over this band and reaches a maximum of about 40% at 7 GHz.

Although the application of the nonlinear theory in the absence of space-charge effects is unphysical for the

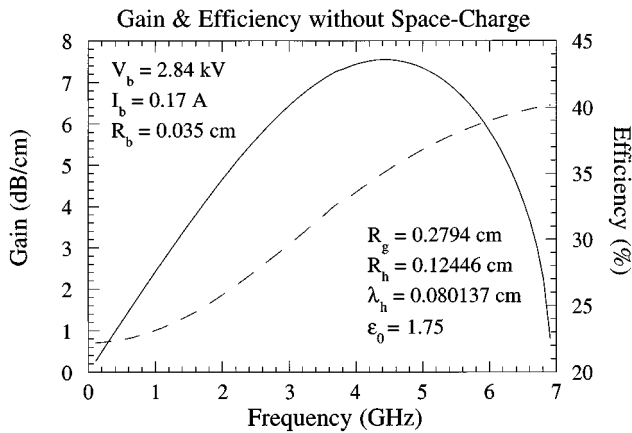


FIG. 8. Plots of the gain (solid line) and efficiency (dashed line) for the parameters of the Northrop–Grumman TWT in the absence of space-charge effects.

Northrop–Grumman TWT, the comparison with the linear predictions in the absence of space-charge affords another test of the validity of the nonlinear model.

We now turn to the nonlinear simulation of this example. For purposes of comparison, we choose the same circuit parameters for the helix, wall, and dielectric constant as used in the cold circuit dispersion comparison in Fig. 6 and in the linear theory in Fig. 8. The beam is assumed to have a continuous pulse structure with a voltage and current of 2.84 kV/0.17 A, and we inject an annular beam with a radius of 0.035 cm. A magnetic field of 950 G was used. The beam rise time is 1 ns. We inject a single pulse of radiation at 5

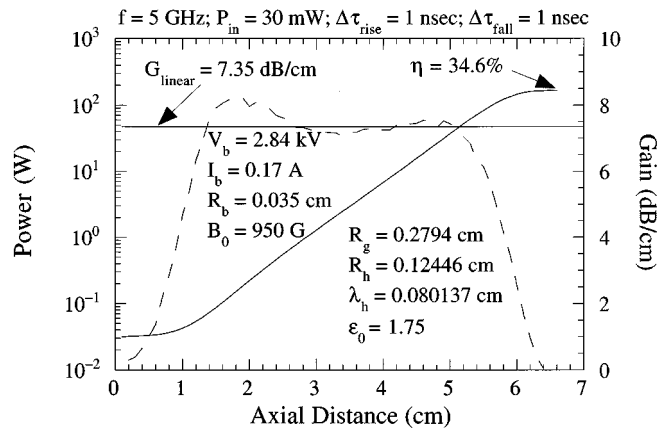


FIG. 9. Plots of the gain (dashed line) and power (solid line) versus axial distance from the nonlinear simulation.

GHz, which is identical to that propagated previously through the vacuum helix with a peak power level of 30 mW, except that we start the pulse after 1 ns (i.e., $\tau_{start}=1$ ns corresponding to the end of the beam rise time), and a 1 ns rise and fall time. The results showing the evolution of the gain and power as a function of axial position are shown in Fig. 9.

It is evident from Fig. 9 that saturation occurs over a length of approximately 6.5 cm at a power level of approximately 167 W for an efficiency of 34.6%. This is in good agreement with the efficiency estimate shown in Fig. 7, which yields an efficiency of about 36% at 5 GHz. As shown in the figure, the linear gain is also in substantial agreement

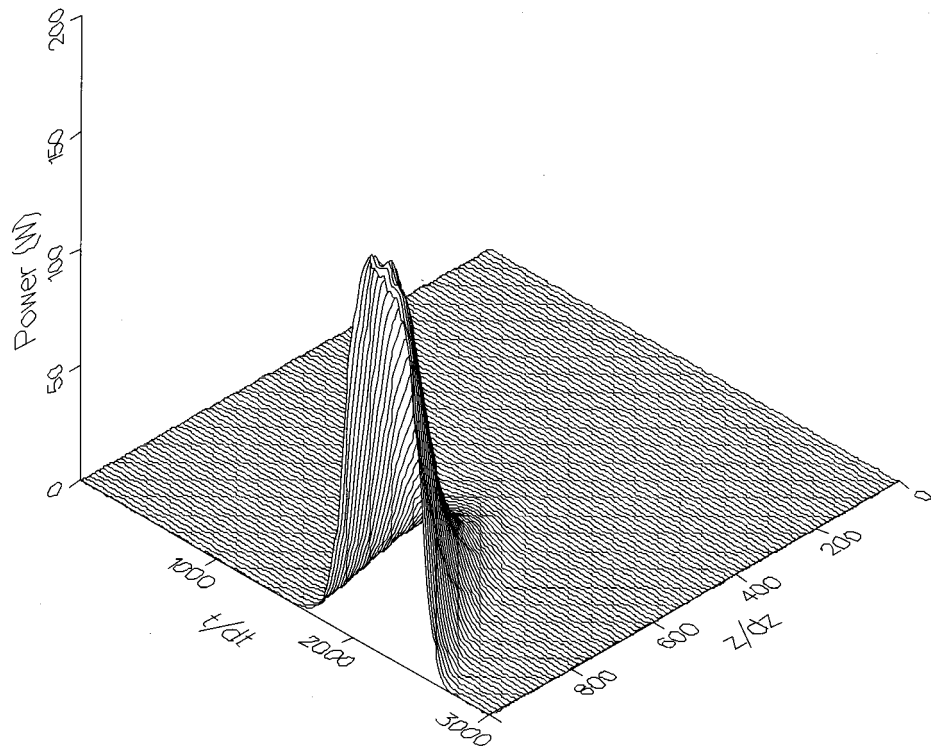


FIG. 10. Perspective plot of the evolution of the injected signal as it propagates through the helix subject to amplification by the beam.

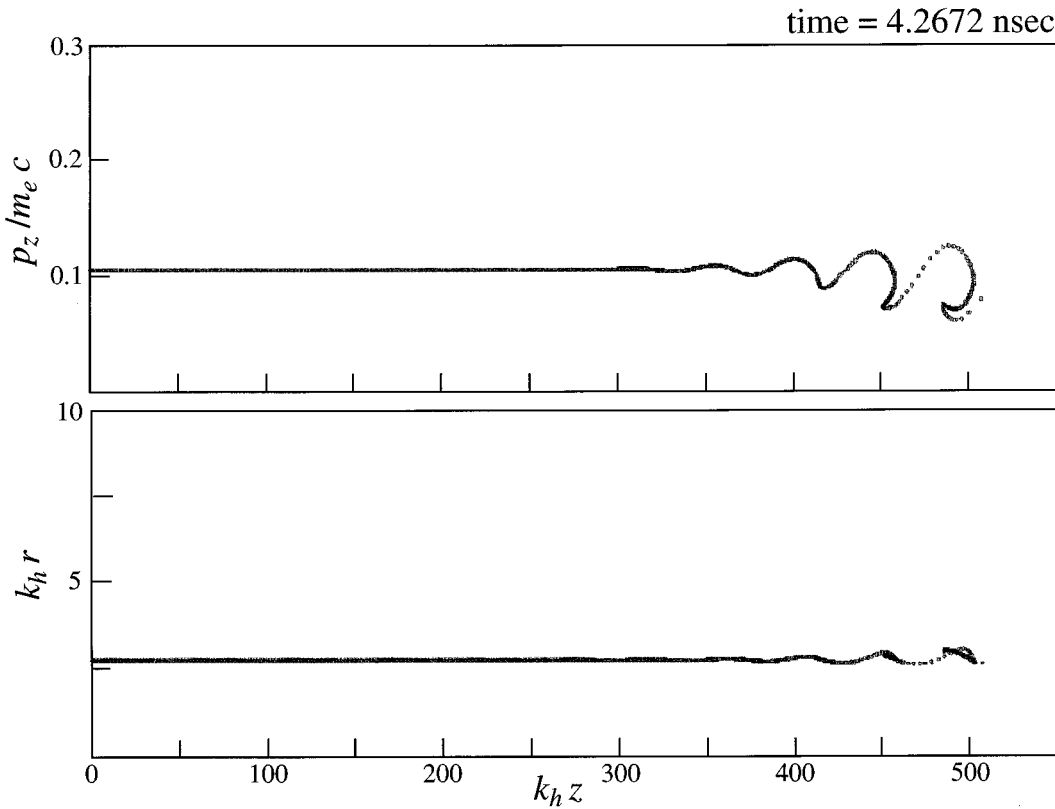


FIG. 11. Plots showing the axial evolution of the phase space and radial structure of electron beam.

with the prediction of the linear theory of a gain of 7.35 dB/cm at 5 GHz. A perspective plot of the evolution of the injected signal as it propagates through the helix subject to amplification by the electron beam is shown in Fig. 10.

Plots of the particle evolution in phase space and in radial position as the beam propagates through the helix are shown in Fig. 11, which is a snapshot of the interaction region once the power has saturated. It is clear from the figure that saturation is by electron trapping in the troughs of the wave and occurs at $k_h z \approx 500$, and that there has been some bunching and overtaking of the beam electrons as they become trapped.

E. Continuous beam case—Tapered helix

In treating a tapered helix, we consider the efficiency enhancements possible for the case considered previously for the uniform helix. The efficiency saturates in a uniform helix after the electrons become trapped in the troughs of the wave, and a state is reached where the number of electrons being decelerated by the wave (and thereby losing energy) is compensated by a similar number of electrons, which are being accelerated by the wave (and gaining energy). At this point the efficiency can be enhanced by decelerating the wave through a downward taper in the helix period. Care must be taken to choose the optimal start-taper point and slope of the taper in order to maximize the rate of efficiency enhancement. The optimum point at which to begin the taper is the point, prior to saturation in the uniform helix, where the electron beam has just become trapped by the wave.

Saturation was found in the uniform helix example considered previously (see Fig. 9) at $z \approx 6.5$ cm, and the nonlinearity in the growth rate begins at $z \approx 5.55$ cm. Hence, we choose this point at which to begin the taper. As a result, we consider an interaction that is identical to that described previously up to $z = 5.5$ cm, after which the helix period will be tapered. The optimum slope of the taper is often not linear, and we choose a two step taper, as shown in Fig. 12, in which $\lambda_h = 0.080\ 137$ cm for $0 \leq z \leq 5.5$ cm after which it decreases linearly in the first step to $\lambda_h = 0.068$ cm at $z = 7.0$ cm, and in the second step down to $\lambda_h = 0.058$ at $z = 10.0$ cm. We now consider the evolution of the signal over this length.

The evolution of the power with axial position is shown in Fig. 13 for the tapered helix. It is evident that the efficiency increases substantially over this length, and reaches a maximum power of approximately 240 W for an efficiency of approximately 50%. The oscillation in the power shown subsequent to the start-taper point with a period of about 1.8 cm corresponds to the bounce period of the electrons trapped in the trough of the wave. The amplitude of the oscillation can be reduced by further optimization on the start-taper point. It should also be noted that even more energy can be extracted from the beam by continuing the taper beyond 10 cm.

The phase space and radial evolution of the electron beam as a function of axial position within the helix are shown in Fig. 14 at 7.0745 ns after the start of the pulse. This corresponds to the time when the peak of the signal exits the interaction region. It is evident from the figure that the beam

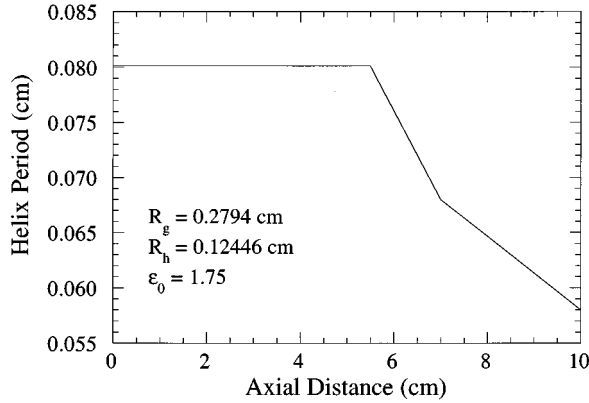


FIG. 12. Variation in the helix period as a function of axial position.

is largely trapped after $k_h z \approx 500$ (i.e., $z = 6.4$ cm) and then decelerates rapidly corresponding to the taper in the helix period. It should be observed that the beam also experiences large-amplitude radial perturbations corresponding to the enhanced energy loss.

F. Emission-gated case

The emission-gated example we consider corresponds to an experiment conducted at the Naval Research Laboratory.²⁴ In contrast to the TWT at Northrop–Grumman, the helix in this case was supported by dielectric posts with a spacing of approximately the helix period and supported at the helix and wall by metallic structures. Thus, the dielectric

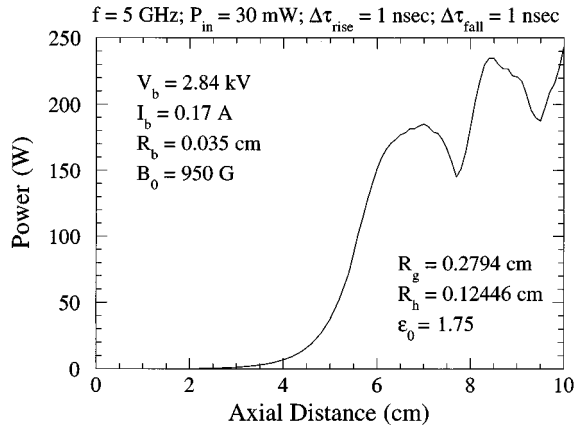


FIG. 13. Plot of the power as a function of axial position for the tapered helix shown in Fig. 12.

supports occupied a much smaller fraction of the volume of the helix/wall gap than was the case for the Northrop–Grumman TWT, and this circuit requires both dielectric and vane loading to model the cold helix dispersion. The wall radius in this case was 3.63 cm and the helix radius and period were 1.4 and 1.966 cm, respectively. Good agreement between the measured dispersion and the cold helix dispersion equation (2) was found for an effective dielectric constant of 1.25 and a vane radius of 3.23 cm. The length of the helix was 33.5 cm. A comparison of the measured and calculated phase velocity as a function of frequency is shown in Fig. 15.

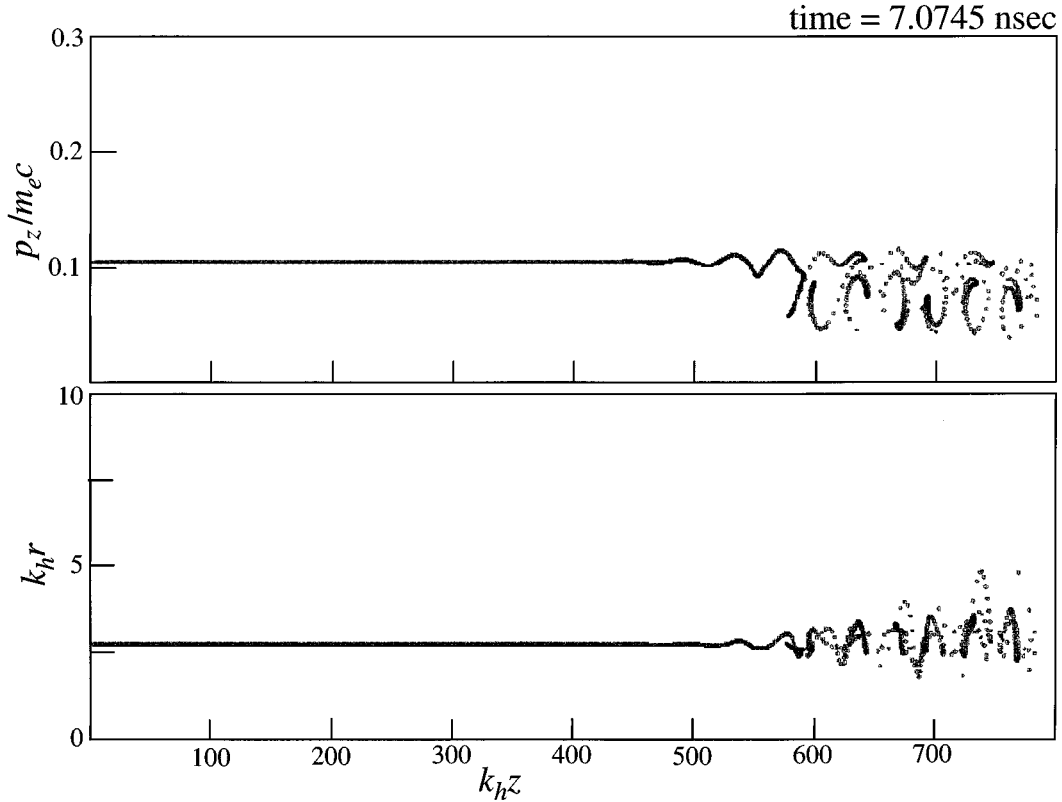


FIG. 14. Plot of the axial evolution of the phase space and radial structure of the beam for the tapered helix interaction.

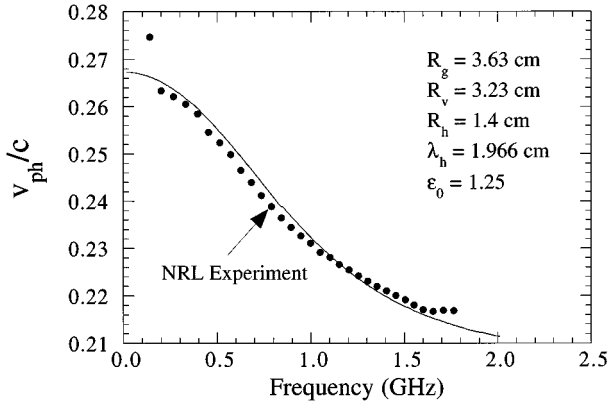


FIG. 15. Comparison of the dispersion as measured in the NRL experiment and as calculated from the dispersion equation (2).

This experiment employed a gridded cathode that was driven at a frequency of approximately 450 MHz. At this frequency, the helix is approximately two wavelengths in length. The specific cases under consideration here used an electron beam with a voltage of 14 kV, a current of 0.1 A, and a radius of 0.508 cm. An external magnetic field of 300 G was imposed. It has been determined from the linear theory that space-charge effects for these beam and circuit parameters do not become important until the current reaches from 1–10 A; hence, we expect that the nonlinear model can treat this experiment. Comparisons between the experiment and simulations bear out this expectation.

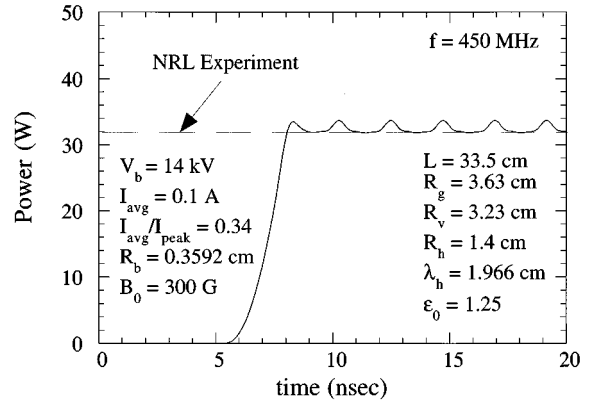


FIG. 16. Evolution of the output power as a function of time for the NRL experiment.

In order to minimize the number of electrons in the simulation (and, hence, minimize run times as well), an annular beam model was assumed with a beam radius of 0.3592 cm (i.e., the rms beam radius). The utility of modeling a solid beam by an annular beam with a radius equal to the rms radius of the solid beam has been demonstrated by means of a linear theory of the interaction.¹⁰ No external drive power was assumed in simulation. We used the beam model shown in Eq. (35) to inject electrons into the interaction region, and studied the variation in the output power as a function of the ratio I_{avg}/I_{peak} .

An example of the temporal evolution of the output

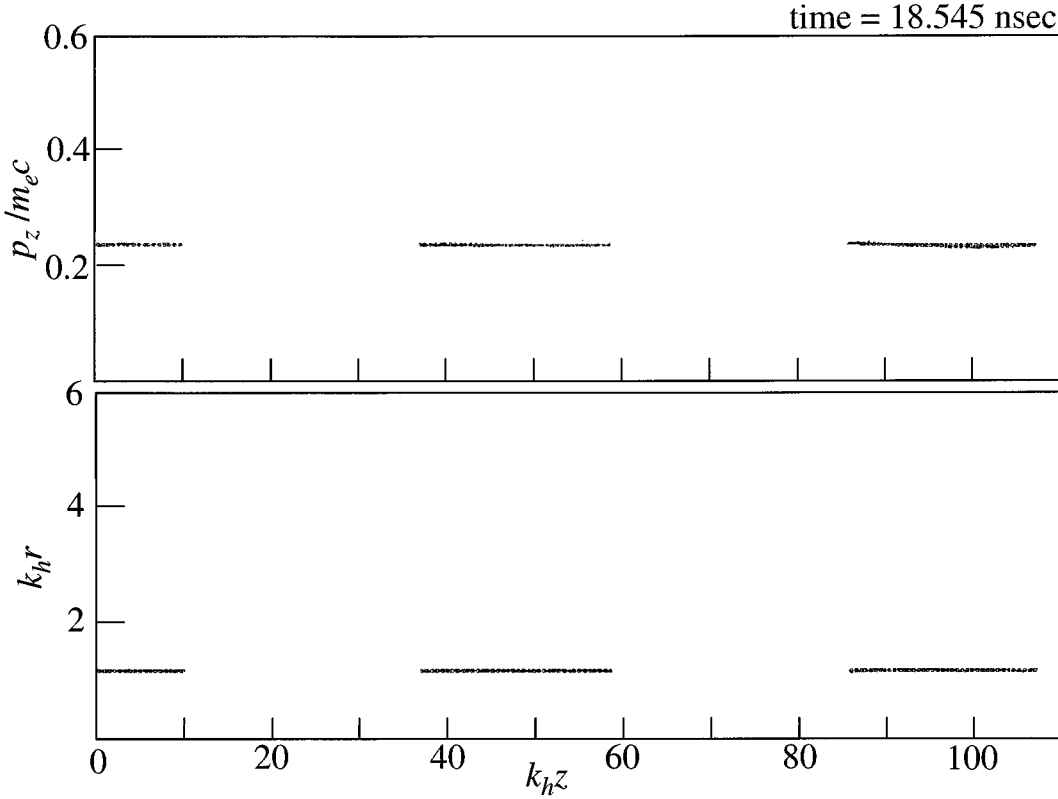


FIG. 17. Plots showing the axial evolution of the phase space and radial structure of the emission-gated electron beam.

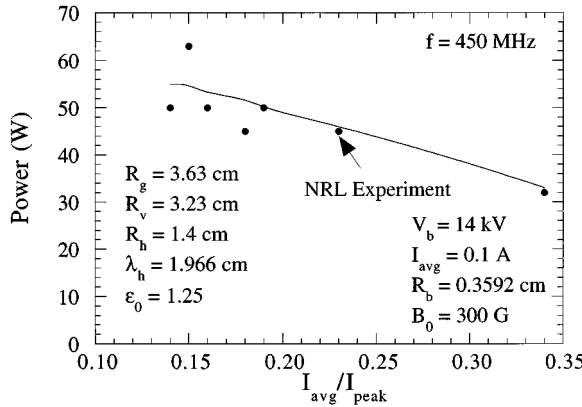


FIG. 18. Comparison of the output power as seen in the experiment and as predicted in simulation as a function of $I_{\text{avg}}/I_{\text{peak}}$.

power is shown in Fig. 16 for $I_{\text{avg}}/I_{\text{peak}}=0.34$. As seen in the figure, there is no output power prior to about 5 ns after the start of the beam pulse, which corresponds to the transit time through the helix. The output power rises rapidly thereafter, however, and rises to its peak value within 2 ns (corresponding to the wave period) and remains relatively constant at a level of approximately 32 W for as long as the beam power is maintained. This corresponds to an efficiency of about 2%, and is in close agreement with the observed output power level of 32 W recorded in the experiment. We also remark that a modulation in the output power at a period of about 2 ns is also observed after the plateau in the output power is achieved. This is a macroscopic effect that stems from the fact that the electron beam is completely bunched at that period and there are vacuum regions between the bunches.

The evolution of the phase space and the radial positions of the beam are shown in Fig. 17 at time well after the output power has plateaued. It is clear that very little energy is extracted from the beam at an efficiency of only 2%; hence, there has been only a marginal growth in the energy spread of the beam, as shown by the slight depression in the axial momentum of the beam electrons near the end of the interaction region.

The level of agreement between the experiment and the nonlinear simulation at $I_{\text{avg}}/I_{\text{peak}}=0.34$ is also found as the ratio of average to peak current is varied. This is shown in Fig. 18 in which the average output power (in the plateau) is plotted versus $I_{\text{avg}}/I_{\text{peak}}$. As shown in the figure, the agreement between the simulation and the experiment is good over a wide variation in the ratio of average to peak currents.

IV. SUMMARY AND DISCUSSION

In this paper, we have described a nonlinear formulation of the interaction of an electron beam and multiple waves in a dielectric- and vane-loaded sheath helix TWT with and without a tapered period. The formulation is in the time domain and is able to treat the propagation of multiple radiation pulses through the helix structure (including the intermodulation between the waves), as well as both continuous and emission-gated electron beams.

The formulation has been compared with linear theories of the interaction as well as with helix TWT experiments, and good agreement has been obtained. It is found that the essential characteristics of the interaction in the helix TWT can be well described by the nonlinear simulation once the effective dielectric constant and vane radius for the helix have been determined. Good estimates of the effective dielectric constant can be obtained using a relatively straightforward volume-weighted average; however, refinements in the estimates of these parameters can be made by comparison of the predicted cold helix dispersion properties with the measured phase velocities of the cold helix.

The fundamental dynamical equation for the fields (27) is quite general in form, and relies largely on a knowledge of the dispersion, polarization, energy density, and Poynting flux for the waves under consideration. Thus, the technique is readily generalized to other configurations and structures. For example, it is straightforward to include reflections at either end of the interaction length and deal with cavities and oscillator configurations. Future work will be directed toward (1) the inclusion of a taper in the helix model, and (2) the treatment of space-charge effects and self-electric and self-magnetic fields. Each of these generalizations is currently in progress.

In view of the computational efficiency and generality of the present formulation to more complex and realistic helix models, the technique has advantages over PIC simulations for treating interactions in helix TWTs.

ACKNOWLEDGMENTS

The authors would like to acknowledge helpful technical discussions with Dr. B. Levush.

This work was supported by the Office of Naval Research and the Office of Naval Technology. The computational work was supported in part by a grant of High Performance Computing (HPC) time from the Department of Defense HPC Shared Resource Center of the Corps of Engineers Waterways Experiment Station (CEWES).

APPENDIX: MODELS IN A DIELECTRIC- AND VANE-LOADED HELIX

We express the components of the electric and magnetic fields in the generic form

$$\delta f = \hat{\delta f}(r) \exp(ikz - i\omega t), \quad (\text{A1})$$

for which Maxwell's equations for the axial components of the electric and magnetic field are

$$[\nabla_\perp^2 + \kappa^2] \begin{pmatrix} \delta \hat{E}_z \\ \delta \hat{B}_z \end{pmatrix} = 0, \quad (\text{A2})$$

where $\kappa^2 \equiv \epsilon(r) \omega^2/c^2 - k^2$ and

$$\epsilon(r) = \begin{cases} 1; & 0 \leq r < R_h, \\ \epsilon_0; & R_h \leq r \leq R_g, \end{cases} \quad (\text{A3})$$

denotes the radial variation of the dielectric coefficient. The transverse components of these fields are given by

$$\delta\hat{E}_r = \frac{ik}{\kappa^2} \frac{\partial}{\partial r} \delta\hat{E}_z, \quad (\text{A4})$$

$$\delta\hat{E}_\theta = -\frac{i\omega/c}{\kappa^2} \frac{\partial}{\partial r} \delta\hat{B}_z, \quad (\text{A5})$$

$$\delta\hat{B}_r = \frac{ik}{\kappa^2} \frac{\partial}{\partial r} \delta\hat{B}_z, \quad (\text{A6})$$

$$\delta\hat{B}_\theta = \frac{i\epsilon(r)\omega/c}{\kappa^2} \frac{\partial}{\partial r} \delta\hat{E}_z. \quad (\text{A7})$$

These equations must be solved subject to the boundary conditions at the helix, vanes, and wall.

In general, the vanes introduce an azimuthal periodicity into the solution that are described by azimuthal harmonics. However, we restrict the analysis to the lowest-order azimuthal harmonic, which describes an azimuthally symmetric solution. Since the electric field components tangent to the surface of the vanes and the magnetic field components normal to the surface of the vanes must vanish, this implies that the azimuthally symmetric solutions in the region of the vanes must be a transverse electric mode with

$\delta\hat{E}_z = \delta\hat{E}_r = \delta\hat{B}_\theta = 0$. For such a case, the effect of the vanes can be modeled by the inclusion of an additional sheath helix at the vane radius for which the period goes to infinity.²⁵ As such, we express the solution for the axial electric and magnetic fields in the form

$$\delta\hat{E}_z = \begin{cases} A_e J_0(pr); & \text{I}, \\ B_e J_0(qr) + C_e Y_0(qr); & \text{II}, \\ D_e W_{0,0}(qR_g, qr); & \text{III}, \end{cases} \quad (\text{A8})$$

and

$$\delta\hat{B}_z = \begin{cases} A_b J_0(pr); & \text{I}, \\ B_b J_0(qr) + C_b Y_0(qr); & \text{II}, \\ D_b W_{1,0}(qR_g, qr); & \text{III}, \end{cases} \quad (\text{A9})$$

where $p^2 \equiv \omega^2/c^2 - k^2$, $q^2 \equiv \epsilon_0 \omega^2/c^2 - k^2$, and we have already imposed the boundary conditions that the transverse components of the electric field and the normal components of the magnetic field must vanish at the waveguide wall at $r = R_g$. Note that the three regions are as defined in Eqs. (3)–(6). Imposing the boundary conditions that $\delta\hat{E}_z$ and $\delta\hat{E}_\theta$ must be continuous at $r = R_h$ and R_v implies that

$$\delta\hat{E}_z = \begin{cases} A_e J_0(pr); & \text{I}, \\ \frac{A_e J_0(pR_h) W_{0,0}(qR_v, qr) - D_e W_{0,0}(qR_g, qr) W_{0,0}(qR_h, qr)}{W_{0,0}(qR_v, qr)}; & \text{II}, \\ D_e W_{0,0}(qR_g, qr); & \text{III}, \end{cases} \quad (\text{A10})$$

and

$$\delta\hat{B}_z = \begin{cases} A_b J_0(pr); & \text{I}, \\ \frac{q A_b J_1(pR_h) W_{1,0}(qR_v, qr) - p D_b W_{1,1}(qR_g, qr) W_{1,0}(qR_h, qr)}{p W_{1,1}(qR_v, qr)}; & \text{II}, \\ D_b W_{1,0}(qR_g, qr); & \text{III}. \end{cases} \quad (\text{A11})$$

Additional boundary conditions at the helix radii are that the tangential components of the electric field at the helix must be perpendicular to the helix, and that the tangential components of the magnetic field parallel to the helix must be continuous. This means that if the helix period goes to infinity then $\delta\hat{E}_z(R_v + 0^\pm) = 0$ and $\delta\hat{B}_z(R_v + 0^-) = \delta\hat{B}_z(R_v + 0^+)$. As a result, the axial components of the fields become

$$\delta\hat{E}_z = A_e \begin{cases} J_0(pr); & \text{I}, \\ \frac{J_0(pR_h) W_{0,0}(qR_v, qr)}{W_{0,0}(qR_v, qr)}; & \text{II}, \\ 0; & \text{III}, \end{cases} \quad (\text{A12})$$

and

$$\delta\hat{B}_z = A_b \begin{cases} J_0(pr); & \text{I}, \\ \frac{q J_1(pR_h) W_{1,0}(qR_g, qr)}{p W_{1,1}(qR_g, qr)}; & \text{II and III}. \end{cases} \quad (\text{A13})$$

Observe that the axial component of the magnetic field is unaffected by the presence of the vanes, while the axial component of the electric field vanishes in the region of the vanes. This yields the transverse-electric polarization in the region of the vanes.

Imposing the same helix boundary conditions at $r = R_h$ implies that

$$\delta\hat{E}_z(R_h + 0^\pm) \sin \phi + \delta\hat{E}_\theta(R_h + 0^\pm) \cos \phi = 0 \quad (\text{A14})$$

and

$$\begin{aligned} \delta\hat{B}_z(R_h + 0^-) \sin \phi + \delta\hat{B}_\theta(R_h + 0^-) \cos \phi \\ = \delta\hat{B}_z(R_h + 0^+) \sin \phi + \hat{B}_\theta(R_h + 0^+) \cos \phi. \end{aligned} \quad (\text{A15})$$

These two conditions imply that

$$A_e J_0(pR_h) \tan \phi = -\frac{i\omega}{cq} A_b J_1(pR_h) \quad (\text{A16})$$

and

$$A_b \tan \phi \left(J_0(pR_h) - \frac{q}{p} J_1(pR_h) \frac{W_{1,0}(qR_g, qR_h)}{W_{1,1}(qR_g, qR_h)} \right) \\ = \frac{i\omega}{cp} A_e \left(J_1(pR_h) + \frac{\epsilon_0 p}{q} J_0(pR_h) \frac{W_{1,0}(qR_h, qR_v)}{W_{0,0}(qR_v, qR_h)} \right). \quad (\text{A17})$$

The dispersion equation (2) is found by setting the determinant of the coefficients in Eqs. (A16) and (A17) to zero, and the field representation in Eq. (1) is obtained by conversion of these fields to a real representation and allowing the amplitude and phase to vary in z and t .

- ¹J. R. Pierce and L. M. Field, Proc. IRE **35**, 108 (1947).
- ²J. R. Pierce, Proc. IRE **35**, 111 (1947).
- ³J. R. Pierce, *Traveling-Wave Tubes* (Van Nostrand, New York, 1950).
- ⁴O. E. H. Rydbeck, Ericsson Techn. **46**, 3 (1948).
- ⁵L. J. Chu and J. D. Jackson, Proc. IRE **36**, 853 (1948).
- ⁶A. H. W. Beck, *Space-Charge Waves* (Pergamon, New York, 1958).
- ⁷R. G. E. Hutter, *Beam and Wave Electronics in Microwave Tubes* (Van Nostrand, New York, 1960).
- ⁸H. P. Freund, M. A. Kodis, and N. R. Vanderplaats, IEEE Trans. Plasma Sci. **PS-20**, 543 (1992).
- ⁹H. P. Freund, N. R. Vanderplaats, and M. A. Kodis, IEEE Trans. Plasma Sci. **PS-21**, 654 (1993).
- ¹⁰H. P. Freund, E. G. Zaidman, M. A. Kodis, and N. R. Vanderplaats, IEEE Trans. Plasma Sci. (in press).
- ¹¹L. Brillouin, J. Appl. Phys. **20**, 1196 (1949).
- ¹²A. Nordsieck, Proc. IRE **41**, 630 (1953).
- ¹³P. K. Tien, L. R. Walker, and V. M. Wolontis, Proc. IRE **43**, 260 (1955).
- ¹⁴J. E. Rowe, IRE Trans. Electron. Devices **ED-3**, 39 (1956).
- ¹⁵J. E. Rowe, *Nonlinear Electron-Wave Interaction Phenomena* (Academic, New York, 1965).
- ¹⁶H. P. Freund and T. M. Antonsen, Jr., *Principles of Free-Electron Lasers* (Chapman & Hall, London, 1992), Chap. 5.
- ¹⁷I. J. Morey and C. K. Birdsall, IEEE Trans. Plasma Sci. **PS-18**, 482 (1990).
- ¹⁸R. J. Faehl, B. S. Newberger, and B. B. Godfrey, Phys. Fluids **23**, 2440 (1980).
- ¹⁹B. Goplen, D. Smith, K. Nguyen, M. A. Kodis, and N. R. Vanderplaats, in *International Electron Devices Meeting Technical Digest* (Institute of Electrical and Electronics Engineers, New York, 1992), pp. 759–762.
- ²⁰H. P. Freund, R. H. Jackson, and D. E. Pershing, Phys. Fluids B **5**, 2318 (1993).
- ²¹G. Groshart, Northrop–Grumman Corp. (personal communication, 1996).
- ²²K. A. Hoffman, *Computational Fluid Dynamics for Engineers* (Engineering Education System, Austin, TX, 1989), p. 171.
- ²³J. C. Slater, *Microwave Electronics* (Van Nostrand, New York, 1950).
- ²⁴M. A. Kodis, N. R. Vanderplaats, E. G. Zaidman, B. Goplen, D. N. Smith, and H. P. Freund, in *International Electron Devices Meeting Technical Digest* (Institute of Electrical and Electronics Engineers, New York, 1994), Catalog No. 94CH35706, pp. 795–798.
- ²⁵D. N. Smith (personal communication, 1996).